PHYSICAL REVIEW A **68**, 030502(R) (2003)

Quantal and classical radiative cascade in Rydberg plasmas

M. R. Flannery[1,2] and D. Vrinceanu[2]
[1]*School of Physics, Georgia Institute of Technology, Atlanta, Georgia 30332, USA*
[2]*ITAMP, Harvard-Smithsonian Center for Astrophysics, Harvard University, Cambridge, Massachusetts 02138, USA*
(Received 4 February 2003; published 11 September 2003)

Atoms in high-(n,ℓ) states formed in cold Rydberg plasmas decay to the ground state in a succession of radiative transitions populating intermediate excited states. A classical treatment presents radiative cascade in a physically transparent way and reveals the ''trajectory'' in $n\ell$ space obeyed by the cascade, scaling rules, and other aspects hidden within the quantal approach. Quantal-classical correspondence in radiative decay is directly demonstrated. Classical transition probabilities are also presented and are in excellent agreement with quantal transition probabilities, even for moderate quantum numbers.

DOI: 10.1103/PhysRevA.68.030502 PACS number(s): 32.70.Cs, 31.15.Gy, 32.30.Jc, 32.80.Rm

Cold Rydberg plasmas, wherein electrons and ions coexist with atoms $R(nl)$ in highly excited Rydberg states n,ℓ have recently been produced by direct laser excitation [1] or ionization [2] of atoms initially prepared at submillikelvin temperatures. In the ATRAP experiment at CERN, levels $n \geqslant 50$ of antihydrogen at 4 K are observed [3]. In these three experiments, the basic processes [4] include three-body recombination which mainly produces Rydberg or anti-Rydberg atoms in high-$\ell \sim n-1$ circular states, which have very long lifetimes $\tau_{n\ell} \sim n^3\ell^2$ towards spontaneous radiative decay. Stark mixing [5] by the electric microfields and collision with ultraslow ions then produce a redistribution of the angular momentum towards much lower ℓ, which, because of the increased electrodynamical $e^- - R^+$ interaction at the pericenter of the highly eccentric orbits, radiate $\sim n^2$ times faster than the high-ℓ states. Theoretical analysis of ultracold Rydberg plasmas involves the distribution of Rydberg atoms over *both* n and ℓ so that the standard collisional-radiative models [6] must be extended. Such an inclusion increases dramatically the computational and numerical difficulties, since the dimension of the required array increases from n^2 to n^4, enough to render direct calculation unfeasible and physical interpretation intractable. Moreover, the well-known Gordon formula [7] for the required radiative transition probabilities becomes numerically unstable for $n \geqslant 50$, even with special numerical algorithms and substantial numerical effort. Some physical transparency is therefore required.

In this paper, we investigate the energy route preferred in radiative cascade of an excited atom in an initially prepared Rydberg level $n\ell$. In so doing, we advance a remarkably accurate classical theory of the subsequent trajectory in $n\ell$ space produced by radiative cascade and illustrate a powerful classical-quantal correspondence at work. A classical treatment of the transition probability (Einstein A coefficient) is also provided. It is worth noting that classical theory of radiative decay was not vigorously pursued after 1930, presumably due to its prediction that the accelerating spiraling electron will ultimately pass through the Coulomb force center, an untenable feature evident for those lowest-n and -ℓ states, the only states then accessible to experimental observation. For high-n states, however, we shall show that the classical picture developed here works remarkably well, even for states with $\ell/n \geqslant 0.2$ which includes the majority of Rydberg states created in the ultracold Rydberg plasmas recently observed [1–3].

The instantaneous classical power of photon emission from an atom with energy E is given by the Larmor formula [8,9]

$$I = \frac{2}{3}\frac{e^2}{c^3}|\ddot{\mathbf{r}}|^2 = -\frac{dE}{dt} = -\mathbf{F}\cdot\dot{\mathbf{r}}, \tag{1}$$

where $\mathbf{F}$ is the (Abraham-Lorentz) force [8] exerted on the atom during photoemission. On assuming that $\mathbf{F}$ is small compared with the Coulomb attraction, then on averaging over the electronic period $T_n = 2\pi n^3 \tau_{au}$, where τ_{au} is the au of time, and following Refs. [8,9], the secular rate of change in quantum number n is given by

$$\frac{dn}{dt} = -\frac{A_0}{\ell^5}\left(1 - \frac{\ell^2}{3n^2}\right), \tag{2}$$

where $A_0 = \alpha_{FS}^3/\tau_{au} = 1.6065 \times 10^{10}\ \mathrm{s}^{-1}$ is the characteristic rate for radiative processes and α_{FS} is the fine-structure constant. The secular rate of change in angular momentum $L = l\hbar$ is obtained upon similar averaging [8,9] as

$$\frac{d\ell}{dt} = -\frac{2}{3}\frac{A_0}{n^3\ell^2}. \tag{3}$$

A classical estimate [10] of the characteristic time $\tau_{n\ell}$ of radiative decay to all lower $n,\ell-1$ states is obtained by equating (3) with $-1/\tau_{n\ell}$ to yield $\tau_{n\ell} = 93.37 n^3\ell^2$ ps. Many orbits occur during radiative decay, since this radiative decay time $\tau_{n\ell} \gg T_n$, the orbital period.

Combining Eqs. (2) and (3) yields

$$\frac{dn}{d\ell} = \frac{3}{2}\frac{n^3}{\ell^3}\left(1 - \frac{\ell^2}{3n^2}\right). \tag{4}$$

Since Eq. (4) is always positive, both n and ℓ change in the same direction, in accord with the quantal propensity rule [6]. The solution of Eq. (4) yields $n^2 = \ell^2/(1 - C\ell^3)$, where the quantity

$$C(n_0,\ell_0) = \frac{1 - \ell_0^2/n_0^2}{\ell_0^3} = \frac{1 - \ell^2/n^2}{\ell^3} \tag{5}$$

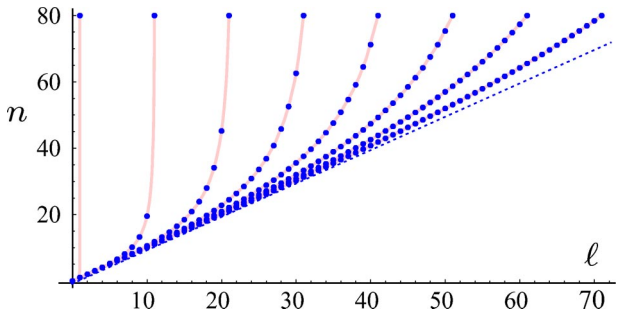

FIG. 1. (Color online) "Trajectories" in (n,ℓ) space for initial states $l_0=1,11,21,31,41,51,61,71$ within the $n_0=80$ shell. Dots correspond to a change of one unit of angular-momentum quantum number $(\Delta\ell=-1)$. The dashed diagonal line $\ell=n$ represents transitions between circular states.

is determined by the initial state $n_0\ell_0$ and remains conserved throughout the radiative cascade process. The $n\ell$ states subsequently populated are illustrated in Fig. 1 where ℓ successively decreases by one unit. Each trajectory is characterized by different values of $C(n_0,\ell_0)$, which can vary between 0, for circular $(\ell_0=n_0)$ states, and 1, for eccentric $(\ell_0=1)$ high-n_0 states. Circular states decay along the diagonal line $(C=0)$ of Fig. 1 as $(n,\ell=n)\rightarrow(n-1,\ell'=n-1)\rightarrow(n-2,\ell''=n-2),\ldots,$ while states with lower angular momentum (and $C>0$) will decay by making increasingly larger jumps

$$\Delta n_c=n-\frac{\ell-1}{\left[1-(1-\ell^2/n^2)\left(\frac{\ell-1}{\ell}\right)^3\right]^{1/2}}, \tag{6}$$

from level n in the $\ell\rightarrow\ell-1$ transition. Direct calculation of the corresponding quantal expression for the averaged change in the principle quantum number

$$\Delta n_q=\left(\sum_{n'=\ell}^{n-1}(n-n')A_{n\ell\rightarrow n'\ell-1}\right)/\sum_{n'=\ell}^{n-1}A_{n\ell\rightarrow n'\ell-1}$$

in terms of probabilities $A_{i\rightarrow j}$ for $i\rightarrow j$ transitions show agreement with the classical prediction (6), even for moderate $n\sim 20$, over an extensive range of ℓ.

Thus, the Bohr correspondence (which predicts $\Delta n=1$ transitions along the diagonal line of circular states) is generalized via Eq. (6) for decay of general noncircular states. Figure 1 also clearly illustrates that any initial orbit will eventually become increasingly circular during the cascade process. The coupled equations (2) and (3) can be solved in analytic form to provide the duration τ of $n_0\ell_0\rightarrow n,\ell$ transitions as

$$A_0\tau=\frac{n_0\ell_0^5}{\left(1+\frac{\ell_0}{n_0}\right)^2}-\frac{n\ell^5}{\left(1+\frac{\ell}{n}\right)^2}. \tag{7}$$

It is worth noting that Eq. (7) predicts $A_0\tau=3n^5/2$ for transitions between circular states, in agreement with the high n limit of the calculated quantal transition rate

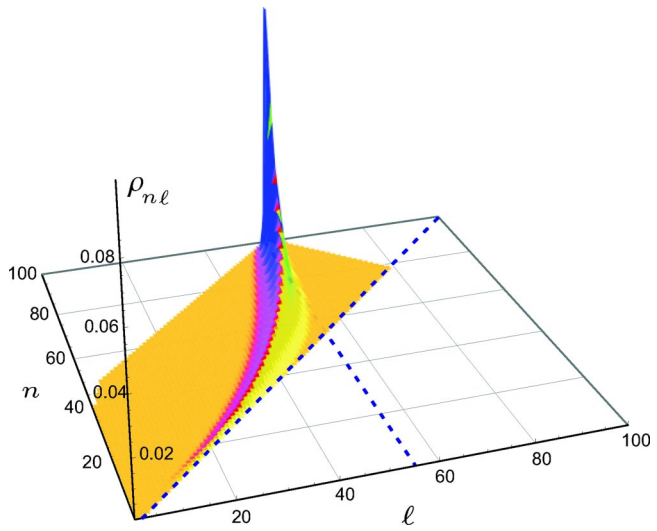

FIG. 2. (Color online) The steady-state quantal distribution $\rho_{n\ell}$ of $n\ell$ states populated by the radiative cascade originating from a source maintained at level $n_0=100$, $\ell_0=55$. The quantal ridge follows the prescribed classical trajectory (5).

$$A_{n,n-1\rightarrow n-1,n-2}=\frac{(2n-1)A_0}{3n^4(n-1)^2}\left[\frac{2^4n^2(n-1)^2}{(2n-1)^4}\right]^n. \tag{8}$$

The set of coupled rate equations for the time-dependent quantal evolution of population $\rho_{n\ell}(t)$ involved in the cascade from the initially populated level (n_0,ℓ_0) are

$$\frac{d\rho_{n\ell}}{dt}=\sum_{n'=n+1}^{n_0}\rho_{n'\ell+1}(t)A_{n'\ell+1\rightarrow n\ell}+\sum_{n'=n+1}^{n_0}\rho_{n'\ell-1}(t)A_{n'\ell-1\rightarrow n\ell}-\rho_{n\ell}(t)\left(\sum_{n'=\ell}^{n-1}A_{n\ell\rightarrow n'\ell-1}+\sum_{n'=\ell}^{n-1}A_{n\ell\rightarrow n'\ell+1}\right).$$

The steady-state solution, subject to the constant source represented as $\rho_{n_0\ell_0}(t)=1$ at all times, is shown in Figs. 2 and 3. It is seen that the quantal distribution over the $n\ell$ plane exhibits (a) a sharp ridge which follows the deduced classical trajectory (5) and is (b) skewed (Fig. 3) towards the left, indicating the predominance of $\ell\rightarrow\ell-1$ downward transitions, in accord with a propensity rule [7]. The quantal-classical correspondence illustrated by Figs. 2 and 3 may be explained as follows. The quantal rate that energy $E_{if}=\hbar\omega_{if}$ is radiated is the power [7]

$$I_{if}=\hbar\omega_{if}A_{if}=\frac{4}{3}\frac{e^2}{c^3}(E_{if}/\hbar)^4|\mathbf{r}_{if}|^2, \tag{9}$$

where $\mathbf{r}_{if}$ is the dipole electronic matrix element $\langle\phi_{n_f\ell_fm_f}|\mathbf{r}|\phi_{n_i\ell_im_i}\rangle$. Since $\ddot{\mathbf{r}}_{if}=-\omega_{if}^2\mathbf{r}_{if}$ exactly, when exact wave functions $\phi_{i,f}$ are used, the total power radiated into all lower states is

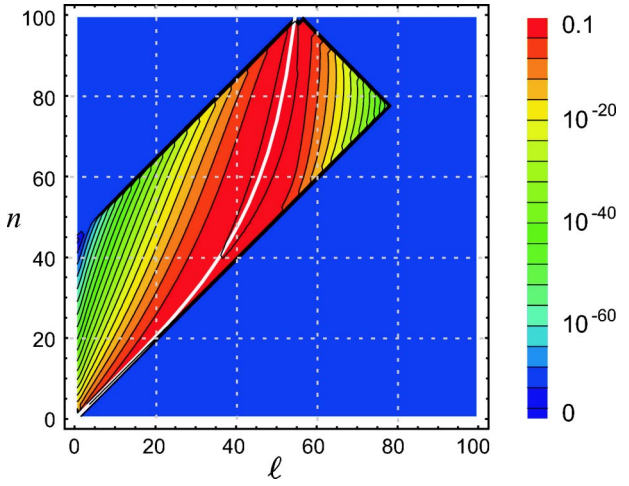

FIG. 3. (Color online) Two-dimensional representation of Fig. 2 but with quantal isodistributions represented by lines with magnitudes determined by each color code on the right hand side. The white line is the classical ridge (5).

$$I_i = \frac{4}{3}\frac{e^2}{c^3}\sum_{f<i}|\ddot{\mathbf{r}}_{if}|^2.$$

The sum $\Sigma_{all f}|\ddot{\mathbf{r}}_{if}|^2 = \langle\ddot{\mathbf{r}}^2\rangle_i$ is dominated by a symmetric band of states centered about the highly excited level i. Then $\Sigma_{f<i}|\ddot{\mathbf{r}}_{if}|^2 = \frac{1}{2}\langle\ddot{\mathbf{r}}^2\rangle_i$ and

$$I_i = \frac{2}{3}\frac{e^2}{c^3}\langle\ddot{\mathbf{r}}^2\rangle_i \tag{10}$$

in agreement with Larmor's theorem (1), from which Eqs. (5) and (6) followed upon a corresponding classical average. The present classical approach based on Eq. (1) is therefore expected to be valid for n and ℓ large enough that radiative decay is confined to within a band of neighboring levels. It is therefore expected to be inadequate for low-ℓ core penetrating electrons where the stronger interactions induce larger quantum jumps to levels outside the band. Based on the success that the quantal ridge in Figs. 2 and 3 follows the energy route classically prescribed by Fig. 1, it is now worthwhile exploring classical rates for $i \to f$ transitions between two discrete levels. The position $\mathbf{r}$ of the electron in initial state $i \equiv n_i \ell_i m_i$ and executing bounded periodic motion with constant angular frequency ω can be Fourier decomposed as

$$\mathbf{r}(i;\theta,\psi,\phi) = \sum_{\mathbf{s}} \mathbf{r}_{\mathbf{s}}(i)\exp i(s_1\theta + s_2\psi + s_3\phi), \tag{11}$$

where the sum is over all $\mathbf{s} \equiv \{s_1, s_2, s_3\}$, where $\theta = \omega t + \delta$ is the angular position of the particle in the orbital plane whose orientation is determined by the constant Euler angles ($\Theta = \cos^{-1} m/l, \phi, \psi$). This permits the time average $\langle I\rangle_{T_n}$ of the Larmor power (1) to be decomposed as $\Sigma_{\mathbf{s}\geqslant\mathbf{0}} I_{\mathbf{s}}$, where each component

$$I_{\mathbf{s}} = \frac{4}{3}\frac{e^2}{c^3}(s_1\hbar\omega/\hbar)^4|\mathbf{r}_{\mathbf{s}}(i)|^2. \tag{12}$$

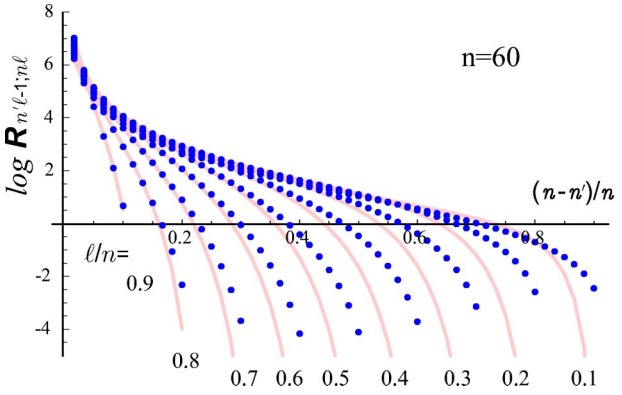

FIG. 4. (Color online) Quantal (blue dots) and classical [(13), red lines] radial matrix elements as a function of scaled change $s/n = (n - n')/n$ for various initial-state ratios ℓ/n from 0.9 to 0.1 in steps of 0.1. The ordinate axis uses a base-10 logarithm.

When compared with Eq. (9), Eq. (12) provides the Bohr [11]-Van Vleck [12] correspondence principle, which equates the power of line spectra between equally spaced levels $E_{if} = s_1\hbar\omega$ (the Bohr frequency theorem [11]) with the power associated with the $\mathbf{s}$th harmonic of the classical motion of state i. The correspondence also holds provided $\mathbf{r}_{if} = \mathbf{r}_{\mathbf{s}}(i)$, where $s_1 = n_f - n_i, s_2 = \ell_f - \ell_i, s_3 = m_f - m_i$, which is the Heisenberg form [13] of a correspondence principle for matrix elements. Since $\mathbf{r}$ is real, $\mathbf{r}_{\mathbf{s}}(i) = \mathbf{r}_{-\mathbf{s}}(i)$, as also assumed within the derivation of Eq. (10). Moreover, $\mathbf{r}_{if} \approx \mathbf{r}_{\mathbf{s}}(i)$ and $\mathbf{r}^*_{fi} \approx \mathbf{r}^*_{-\mathbf{s}}(f)$, where i or f denote taking the parameters for the initial or final orbits, respectively. For $i = n_i\ell \to f = n_f\ell \pm 1$ transitions, calculation of the Fourier coefficients $\mathbf{r}_{\mathbf{s}}(j)$ in Eq. (11) for the initial and final classical orbits $j = i, f$ then provides the new correspondence

$$|\mathbf{r}_{if}|^2 = \mathbf{r}_{if}\mathbf{r}^*_{fi} \approx \mathbf{r}_{\mathbf{s}}(i)\mathbf{r}^*_{-\mathbf{s}}(f) = \frac{\ell_>}{2\ell+1}R_i(s)R_f(s), \tag{13}$$

which is symmetrical with respect to the "classical" radial matrix elements

$$R_j(s) = \frac{a_j}{2s}\left[\left(1 - \Delta\ell\frac{\ell_j}{n_j}\right)J_{s-1}(s\epsilon_j) - \left(1 + \Delta\ell\frac{\ell_j}{n_j}\right)J_{s+1}(s\epsilon_j)\right].$$

Here $a_j = n_j^2 a_0, \epsilon_j = (1 - \ell_j^2/n_j^2)^{1/2}$, $s = (n_i - n_f) > 0$, $\Delta\ell = \mp 1$, and $J_{s\pm1}$ are Bessel functions of order $s \pm 1$. Since $R_i(s)R_f(s)$ in Eq. (13) is our classical representation of the standard [7] quantal radial matrix element $R^2_{n_i\ell, n_f\ell\pm1}$, then under radial correspondence alone, our classical version of the A coefficient for $i \to f$ transitions in Eq. (9) is, therefore,

$$A_{n_i\ell_i \to n_f\ell_f} = \frac{4A_0}{3}\frac{\ell_>}{2\ell+1}\left(\frac{n_i^2 - n_f^2}{2n_i^2 n_f^2}\right)^3 R_i(s)R_f(s), \tag{14}$$

where only the Heisenberg correspondence $\mathbf{r}_{if} \approx \mathbf{r}_{\mathbf{s}}(i)$ and $\mathbf{r}^*_{fi} \approx \mathbf{r}^*_{-\mathbf{s}}(f)$ is used. Expressions (13) and (14), symmetric in the initial and final states, are proved to be valid and much more accurate over a much more extensive range of $s = (n_i - n_f)$ than those obtained [14] from the assumption in Eq. (12) that $|\mathbf{r}_{if}|^2 \approx R_i(s)^2/2$. This distinction, as derived in the

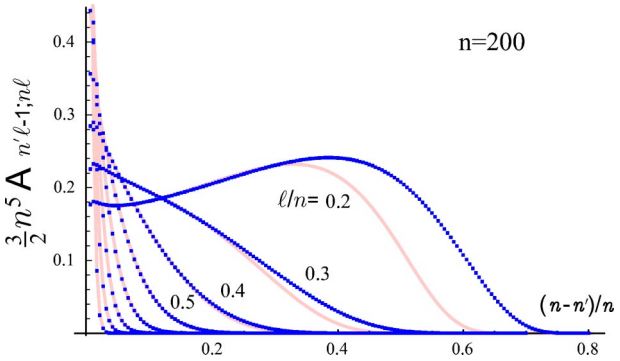

FIG. 5. (Color online) Quantal (blue dots) and classical [(13), red lines] transition rates $A_{200\ell\to n'\ell-1}$ times $\tau_{n,n\to n-1,n-1}=3n^5/2A_0$, as a function of $(n-n')/n$ for various initial scaled angular-momentum values ℓ/n from 0.9 to 0.2 in steps of 0.1.

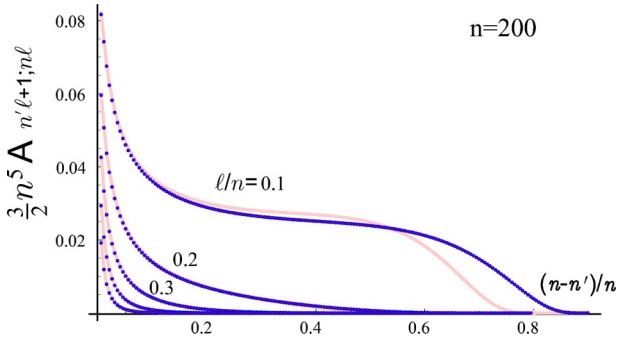

FIG. 6. (Color online) As in Fig. 5, but for $[200,\ell\to n',(\ell+1)]$ transitions for $\ell/n=0.1-0.5$.

new correspondence (14) is important, particularly for intermediate and large values of s when the approximation $R_i(s)\approx R_f(s)$ breaks down, being valid only for $s\sim 1,2,3$. Figure 4 for $n\ell\to n'(\ell-1)$ transitions shows that the quantal and classical radial matrix elements, $R^2_{n\ell,n'\ell\pm1}$ are in excellent agreement over an extensive range in $s=n-n'$ as ℓ is varied from $0.9n$ to $0.1n$. Figure 4 illustrates also that the stronger e-ion interaction at the pericenter for low ℓ orbits induces transitions over a broader range of s, in contrast to transitions with small s characteristic of near circular (higher ℓ) orbits.

The quantal and classical transition probabilities are compared in Figs. 5 and 6 for $\ell\to\ell\mp1$ downward transitions. The agreement is excellent, particularly for large angular momenta, circular states, in accord with Bohr's $\Delta n=1$ correspondence. It is less good for elongated states with low angular momenta (which favor larger n changes) because the equally spaced levels approximation within the Heisenberg correspondence becomes less accurate and because the E^3_{if} factor in Eq. (14) amplifies any error in $R_{i,f}(s)$. Note that the probabilities for $\ell\to\ell-1$ downward transitions are much higher by a factor of 10^2 than those for $\ell\to\ell+1$ transitions, as illustrated also in Figs. 2 and 3. The extent of quantal-classical agreement shown in Figs. 2–6 is representative for all $n\geqslant 10$. The present classical radiative rates are much easier to evaluate correctly than their quantal counterparts.

In summary, the classical treatment of radiative decay outlined here has proven to be accurate, particularly for Rydberg states with $\ell/n\geqslant 0.1$ (preponderant in recombination) and has provided an accurate yet physically transparent picture of radiative cascade of Rydberg states. The deduced trajectory in $n\ell$ space obeyed by radiative cascade origination from a constant source is confirmed by quantal calculation. The deduced classical invariant (5) has, as yet, no quantal analog, indicating a hidden symmetry. The theory is further developed, via Eq. (13) in Eq. (9), to provide here a symmetrized new version of the power correspondence (12) and a classical version (14) of Einstein transition rates, to a high degree of accuracy. It is particularly appropriate for the analysis of Rydberg plasmas over (n,ℓ) and for the proposed deactivation of the high $n\geqslant 50$ states in the ATRAP experiment by laser deexcitation methods, subjects of intense current theoretical and experimental interest.

This work was supported by AFOSR Grant No. 49620-02-1-0338 and NSF Grant No. 01-00890 and by a NSF Grant to ITAMP at the Harvard University-Smithsonian Astrophysical Observatory.

[1] M.P. Robinson *et al.*, Phys. Rev. Lett. **85**, 4466 (2000).
[2] T.C. Killian *et al.*, Phys. Rev. Lett. **86**, 3759 (2001).
[3] G. Gabrielse *et al.*, Phys. Rev. Lett. **89**, 213401 (2002).
[4] M.R. Flannery and D. Vrinceanu, in *Atomic Processes in Plasmas*, edited by E. Oks and M.S. Pindzola (AIP Press, New York, 1998), pp. 317–333.
[5] D. Vrinceanu and M.R. Flannery, Phys. Rev. **63**, 032701 (2001).
[6] B. Zygelman, J. Phys. B **36**, L31 (2003)
[7] H.A. Bethe and E.E. Salpeter, *Quantum Mechanics of One-and Two-Electron Atoms* (Plenum, New York, 1977), pp. 262, 259, and 250.
[8] J.D. Jackson, *Classical Electrodynamics* (Wiley, New York, 1998), p. 770.
[9] L.D. Landau and E.M. Lifshitz, *The Classical Theory of Fields* (Pergamon, Oxford, 1987), p. 187.
[10] K. Omidvar, Phys. Rev. **26**, 3053 (1982); E.S. Chang, *ibid.* **31**, 495 (1985); H. Marxer and L. Spruch, *ibid.* **43**, 1268 (1991).
[11] N. Bohr, in *Sources of Quantum Mechanics*, edited by B.L. Van der Waerden (Dover, New York, 1968), p. 95.
[12] J.H. Van Vleck, Phys. Rev. **24**, 330 (1924).
[13] W. Heisenberg, Z. Phys. **33**, 879 (1925); in *Sources of Quantum Mechanics* (Ref. [11]), p. 261.
[14] P.F. Naccache, J. Phys. B **5**, 1308 (1972); I.C. Percival and D. Richards, Adv. At., Mol., Opt. Phys. **11**, 1 (1975).